Hydrothermally Synthesized NiS_2 and $NiSO_4(H_2O)_6$ Nanocomposites and its Characterizations

Ayushi Sharma[1], Shreya[1*], Peeyush Phogat[1], Ranjana Jha[1], and Sukhvir Singh[1]
[1]Research Lab for Energy Systems, Department of Physics, Netaji Subhas University of Technology, New Delhi, INDIA
*shreyasharma.aug15@gmail.com

Abstract. The present manuscript discusses an in-depth explanation of the synthesis and characterization of nickel sulphide (NiS_2) and nickel sulphate [$NiSO_4(H_2O)_6$] nanocomposites. The phase analysis was performed through x-ray diffraction (XRD), revealing the presence of NiS_2 and $NiSO_4(H_2O)_6$ nanocomposites, along with the presence of deuterium. The synthesized material exhibited absorbance in the visible region, with an optimized band gap of 1.0 eV. The presence of carbon spheres was confirmed through morphological analysis performed through field emission scanning electron microscopy (FESEM), depicting the growth of NiS_2 on the surface of carbon spheres and the presence of nanosheets of $NiSO_4(H_2O)_6$. These techniques provide a detailed explanation of the crystallite size for the nanocomposites, their structural properties and optical properties. The material showed a narrow band gap making it highly suitable for solar cell applications.

Keywords: nanocomposite, center of inversion, phase transition, anorthic.

1 Introduction

Over the previous years, there has been rapid development in material science for the application of renewable energy. Renewable energy can involve materials for capacitors used in charge storage or for solar cells to achieve higher efficiency. Nanocomposites, due to their beneficial qualities [1] such as increased thermal stability (useful in situations where temperature control and resistance to heat are essential), increased surface-to-volume ratio (advantageous in sensing, adsorption, and catalysis applications [2]), and increased or decreased bandgap (essential in solar systems [3]), have gained a lot of interest in the field of solar materials.

One of the widely explored compounds is NiS_2, which depicts allotropy, including hexagonal and cubic forms. NiS_2 has a bandgap of 0.5 eV but due to its smaller bandgap the material does not represent an

optimum band gap for solar spectrum. To overcome the challenge, the present experiment has been performed in which the nanocomposites of nickel sulphide (NiS_2) and nickel sulphate [$NiSO_4(H_2O)_6$] were fabricated having a bandgap of 1.0 eV. The introduction of nanoscale nickel sulfide into a matrix of nickel sulphate can improve electrical conductivity, making it suitable for use in supercapacitors and solar cells[4]. The presence of nickel sulfide nanoparticles can affect the optical characteristics of nanocomposites[5]–[7], which is crucial for applications requiring customized optical properties, such as sensors, optical gear, and coatings. Nickel sulfide is also well-known for its catalytic properties[8],[9] and application in energy storage devices [10]. Moreover, nickel sulfate hydrate likewise offers potential advantages in the development of batteries, in catalysis [2], as an electrolyte for batteries, and for the treatment of wastewater, nickel sulfate hydrate is frequently employed. Therefore, the goal of this study was to uncover all of these benefits in a single sample [1].

2 Experimental Information

2.1 Chemical Used

Table 1 lists all compounds that were used during synthesis along with their purity percentage. All the cleaning and washing were done using deionized water (DI water) and absolute ethanol. All the solutions were prepared in DI water.

Table 1

Chemical Name	Company	Purity percentage
Nickel Acetate	LOBA Chemie	98%
Thiourea	M/s Sigma-Aldrich Pvt. Ltd.	≥99%

2.2 Synthesis

Synthesis and characterization of as-synthesized carbon nanospheres were published elsewhere [11]. Typically, 0.5M of D-Glucose was dissolved in 100 ml DI and stirred for 30 min at 22°C. Then the solution was placed autoclave for 6 hours at 200°C. Afterwards on cooling the solution was cleaned thrice by DI and ethanol, which was further transferred to a vacuum oven for drying at 60°C for one day. In the end, the sample was grinded to obtain carbon spheres. Initially,

0.07 g of carbon nanospheres were dispersed in 30 ml ethanol. This mixture was placed in a bath sonicator for 15 minutes to make the solution volatile. After sonication, the solution was stirred for the next 20 minutes. Additionally, a solution of 0.6 M (2.2 g) thiourea was prepared using 50 ml DI water. At the same time, a third solution of 0.04 M (0.35gm) nickel acetate was stirred in 50 ml ethanol. The solutions containing thiourea and carbon nanospheres were added dropwise into the nickel acetate solution. The final solution was then heated at 200°C for 24 hours in a steel autoclave with Teflon covering. Afterwards, the sample was left overnight to cool down naturally. Then, it was centrifuged and washed three times with DI water and ethanol respectively. Following this, the solution was then placed in a vacuum oven to dry at 70°C for 24 hours. The final sample was obtained by grinding till fine powder was procured.

3 Results and Discussion

3.1 Characterization Details

For the identification of the phase and the structure, X-Ray Diffractometer (make: Rigaku, model: Smartlab 3kW), was used. The X-ray diffraction pattern was captured using copper (Cu) K-radiation (=1.5406 Å). The morphological and elemental content of the sample was analyzed using a FESEM (make: JEOL, model:7610FPlus). To capture the optical response, a Shimadzu UV-2600i UV-Vis spectrophotometer was employed.

3.2 X-Ray Diffraction

The X-ray diffraction pattern of the as-synthesized sample was recorded in a range of 2θ from 10° to 70°. A part of these identified peaks showed a good match with JCPDS file: ***01-073-0574*** illustrating the development of nickel sulfate hydrate with Miller indices in the planes (110), (-112), (112), (-202), (-114), (-110), (115), (022), (220), (200), (222), (0-12), (-119), (-133), (113), (136), (1211), (-428), (-110), (-1114) and (-247). The remaining peaks were also analyzed and indexed with JCPDS file: ***01-079-0105,*** corresponding to nickel sulfide with Miller indices in planes (-202), (-1-31), (-320) and (2-31). Fig. 1. depicts the XRD pattern demonstrating the development of the nanocomposites of nickel sulfate hydrate and nickel sulfide, having monoclinic and anorthic structures respectively. Nickel sulfide hydrate was found to have space group C2/c and space group number 15, exhibiting the existence of a center of inversion, a 2-fold rotation axis and a mirror plane perpendicular to that axis. Nickel sulfide was

observed to have space number 1 and space group P1, revealing a triclinic crystal system with no additional symmetry element beyond translation symmetry. No carbon peak was observed in the XRD pattern due to the trace amount of carbon nanospheres present in the as-synthesized sample.

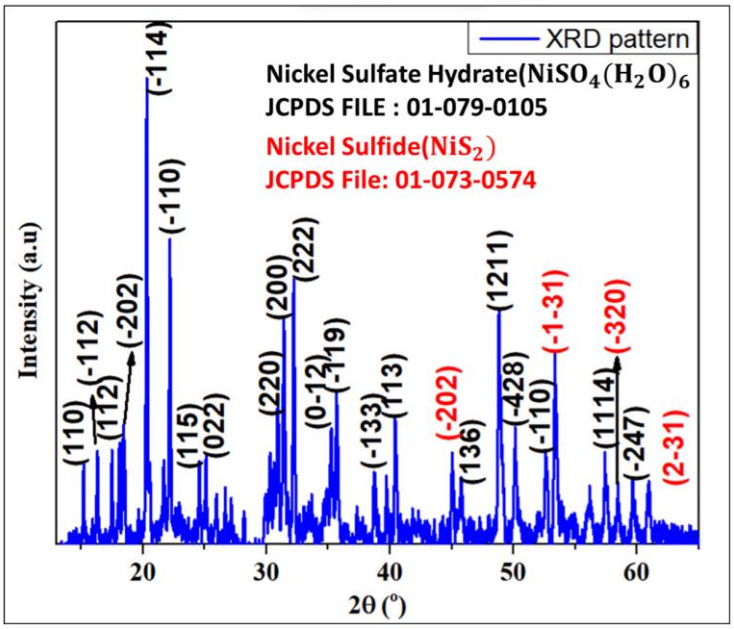

Fig. 1. XRD spectra of as synthesized $NiS_2/NiSO_4(H_2O)_6$ nanocomposites.

3.2.1 Lattice Parameters, Crystallite Size and Strain

Calculation of lattice parameters of as-synthesized sample with the help of equations given below:

$$\frac{1}{d_{hkl}{}^2} = \left[\frac{h}{a}\begin{bmatrix}\frac{h}{a} & cos\gamma & cos\beta\\ \frac{k}{b} & 1 & cos\alpha\\ \frac{l}{c} & cos\alpha & 1\end{bmatrix} + \frac{k}{b}\begin{bmatrix}1 & \frac{h}{a} & cos\alpha\\ cos\gamma & \frac{k}{b} & cos\alpha\\ cos\beta & \frac{l}{c} & 1\end{bmatrix}\right.$$
$$\left. + \frac{l}{c}\begin{bmatrix}1 & cos\gamma & \frac{h}{a}\\ cos\gamma & 1 & \frac{k}{b}\\ cos\beta & cos\alpha & \frac{l}{c}\end{bmatrix}\right] . \begin{bmatrix}1 & cos\gamma & cos\beta\\ cos\gamma & 1 & cos\alpha\\ cos\beta & cos\alpha & 1\end{bmatrix}$$

(for anorthic) .....(1)

$$\frac{1}{d_{hkl}^2} = \frac{h^2}{a^2 sin^2\gamma} + \frac{k^2}{b^2 sin^2\gamma} - \frac{2hkcos\gamma}{absin^2\gamma} + \frac{l^2}{c^2} \text{ (for monoclinic)} \quad .....(2)$$

Here, d shows interplanar spacing, a, b and c denote lattice parameters of crystal and hkl are the miller indices.

Table 2 lattice parameter of synthesized material matched with JCPDS parameters.

Lattice parameter	**JCPDS Value (01-073-0574)**	**As synthesized (NiS_2)**	**JCPDS Value (01-079-0105)**	**As synthesized $NiSO_4(H2O)_6$**
a(Å)	5.6849(Å)	5.77(Å)	9.88(Å)	9.578(Å)
b(Å)	5.6849(Å)	5.6839(Å)	7.228(Å)	7.2448(Å)
c(Å)	5.6849(Å)	5.621(Å)	24.13(Å)	27.06(Å)

The crystallite size of the as synthesized nanocomposite was determined with the help of Debye Scherer formula [8], [9], [12] given in equation- 3 below as,

$$D = \frac{K\lambda}{\beta Cos\theta} a \qquad \text{.....(3)}$$

Here, D is crystal grain size, λ is the wavelength of x-ray (0.154nm), K is constant with value 0.9 known as Scherer constant, β is FWHM and θ is angle at which FWHM is obtained from XRD data. The average crystallite size was computed by considering all analyzed peaks. Therefore, the crystallite size from the above data was 65 nm. The Debye Scherer equation was based on the fact that there was no strain, which might not be the case with the as-synthesized material. Consequently, additional techniques such as Williamson-Hall plot and the Size-Strain plot, were attempts to precisely determine the crystallite size of the material.

The above table.2 confirmed that there was deviation of the computed value from the standard one due to the presence of micro and lattice strain in the material. Williamson Hall plot, a well-known approach, was used to determine the strain as well as the shifted crystallite size due to the presence of strain. According to the Williamson-Hall plot (W-H plot), both strain and crystallite size attributed to the enlargement of XRD peaks. The equation of W-H plot [1] is given by eqn.(4),

$$\beta_T Cos\theta = (\varepsilon \times 4Sin\theta) + \frac{K\lambda}{D} \qquad \text{.....(4)}$$

Here, β_T is FWHM, ε is strain, θ is the angle, K is Scherrer constant possessing the value 0.9, λ is wavelength of X-ray (0.154nm), D is crystallite size. Williamson Hall plot is shown by fig. 2(a), with the value of calculated slope and strain. From the intercept and slope of this plot crystallite size was determined to be **95.5 nm** and strain (ε) was found to be $\mathbf{8.8\times10^{-4}}$**.**

In the Williamson-Hall plot, the observed randomness was attributed to

the Full Width at Half Maximum (FWHM) value. To mitigate this randomness, SS plot was considered as the data represents average FWHM.

Additionally, the material's crystallite size and strain were accurately determined through the size-strain plot. The equation used for size strain plot [13]is as follows,

$$(d_{hkl}\beta_{hkl}cos\theta)^2 = \frac{k\lambda}{t}\beta_{hkl}d^2{}_{hkl}cos\theta + \frac{\varepsilon^2}{4} \quad \text{.....(5)}$$

Hence, the calculated crystallite size and strain was found to be **132 nm** and **10.9×10^{-4}** respectively**.**

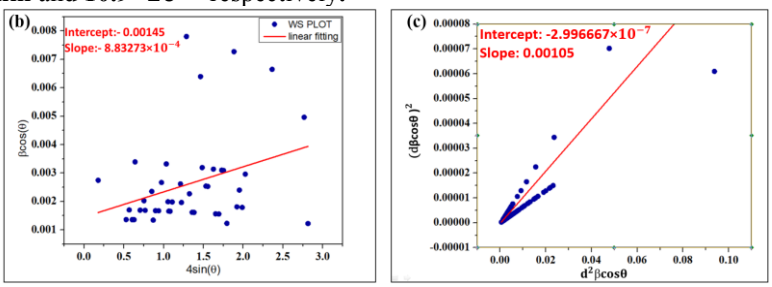

Fig. 2. (a) Williamson Hall plot, (b) size strain plot.

Table 3 crystallite size and strain by various methods.

	Debye Scherrer	**Williamson Hall**	**Size-Strain**
Crystallite size	**65.4 nm**	**95.5 nm**	**132 nm**
strain	**--**	**8.8×10^{-4}**	**10.9×10^{-4}**

3.3 UV-Vis Spectroscopy

With the aim to investigate optical properties of the synthesized nanocomposites, UV-visible spectroscopy was recorded in the range of 190 nm to 850 nm as shown in Fig. 3. (a). The UV-visible spectra showed that the nanocomposites revealed high absorbance in the visible region from 300 nm to 820 nm. The maximum absorbance was recorded at a peak 531.5 nm.

To study whether the as-prepared sample is an insulator, conductor, or semiconductor, the optical bandgap was calculated. Bandgap is the difference of energy between the conduction and valance band Fig.3.(b) shows the Tauc plot [1] through which the bandgap of the as-prepared sample was calculated. Here, Beer Lambert's law was applied which is given as [14] :

$$\alpha h\nu = A[h\nu - E_g]^{1/n} \quad \text{....(6)}$$

Here, A represents the absorbance coefficient; E_g symbolizes the direct band gap; α shows the molecular extinction coefficient; h is Plank's

constant; v is frequency; for a direct band gap n corresponds to ½, whereas for an indirect band gap, it's equal to 2.
The computed bandgap was 1.06 eV**.** Materials with a bandgap of approximately 1 eV offer various benefits, such as being ideal for solar absorption, thermophotovoltaics, infrared sensing and imaging, optoelectronics, catalysis, and photocatalysis as well as energy harvesting. Making them perfect for applications in solar cells, thermophotovoltaic devices, infrared sensing and imaging, LEDs, visible light photocatalysis, semiconductor devices, thermal photovoltaics, and energy harvesting.

3.3.1 Refractive index

Various materials or phases in a material show distinct refractive indices. The speed that light travels for a specific sample relative to the speed of light in a vacuum is referred to refractive index. The refractive index was computed to understand the application of the sample in thin film optics, and sensors, and to assess its optical properties. The formula used to calculate the refractive index [13] of the prepared sample

$$\frac{n^2-1}{n^2+2} = 1 - \sqrt{\frac{E_g}{20}} \quad \ldots\ldots(7)$$

Here, n= refractive index, E_g=band gap, so the calculated refractive index of the sample was 3.32. The refractive index value of 3.32 for NiS_2 and $NiSO_4(H_2O)_6$ nanocomposites in solar cell applications can enhance light absorption, improve optical matching, and optimize photogenerated carrier separation. These nanocomposites can be incorporated into light-trapping structures, enhancing absorption and conversion efficiency. They can also contribute to bandgap engineering, allowing for materials with specific energy levels aligned with the solar spectrum. Additionally, nanocomposites can increase the solar cells' stability and lifespan, making them cost-effective compared to traditional materials. However, the specific benefits depend on the nanocomposites' structure, composition, and morphology. To assess these nanocomposites' efficiency and viability in solar cell applications, more investigation and validation through experimentation are required.

3.3.2 HOMO LUMO levels

HOMO, or Highest occupied molecular orbital, is commonly known as the valence band, whereas LUMO, or Lowest unoccupied molecular orbital, is commonly known as the conduction band. Calculating the HOMO and LUMO offers insights into the chemical reactivity, charge transfer processes, optical properties, semiconductor properties, drug design, catalytic activity, material properties, stability, energy storage, and solar cell efficiency. The HOMO-LUMO gap is crucial in nucleophilic reactions, charge transfer processes, optical properties,

semiconductors, drug design, catalytic activity, material properties, and energy storage. Understanding these orbitals is essential for designing molecules with specific reactivity, influencing reaction pathways and efficiency, optimizing charge storage and release processes, and enhancing solar cell efficiency. Thus, calculating HOMO and LUMO provides a foundation for comprehending the electronic properties of molecules and materials, enabling informed decisions in various scientific and technological applications.

Equations used to calculate HOMO and LUMO are as follows [15],

$$E_{VB} = \chi - E_e + 0.5\, E_g \quad \text{.....(8)}$$

$$E_{CB} = E_{VB} - E_g \quad \text{.....(9)}$$

For nickel sulfide, valance band was found to be 1.26 eV, and the conduction band was 0.2 eV. For nickel sulfate hydrate valance band was -1.17 eV, and the conduction band was -2.23 eV.

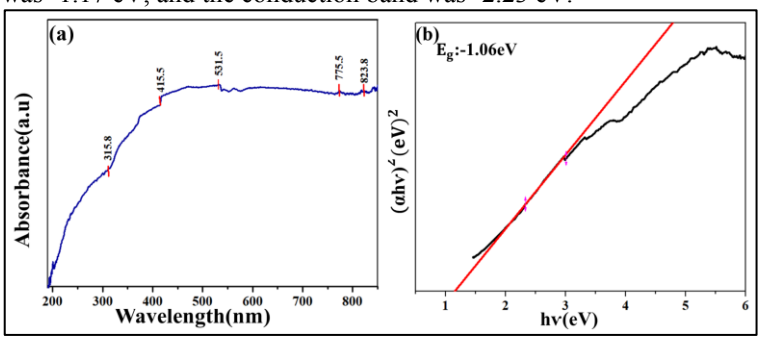

Fig. 3. (a) absorbance spectra of nanocomposites, (b) Tauc plot.

3.4 Morphological Analysis

Although XRD does not confirm the presence of carbon in the synthesized sample, FESEM images revealed that the as-synthesized sample contains carbon spheres. Fig.3 (a) depicts the carbon spheres with particle size near 400 nm range. The image depicts the growth of smaller particles of nickel (either sulfide or sulphate) growing on the surface of the carbon. However, for most of the morphology, the material depicts the growth of sheets caused due to the agglomeration of smaller particles of $NiSO_4(H_2O)_6$. The irregular morphology of 2D Nano sheets will enhance the optical properties of the material whereas the nanospheres will provide better stability to the material.

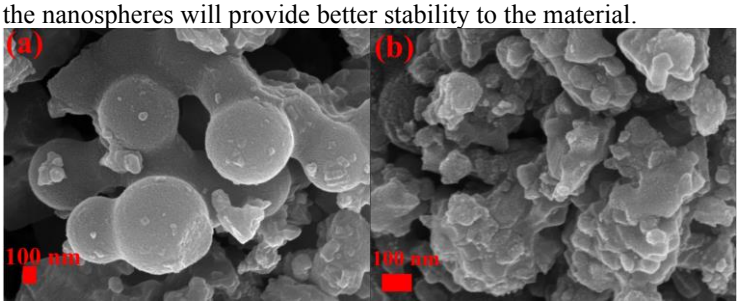

Fig. 4. FESEM images at two different scales.

4 Conclusion

The current work focused on the synthesis of nanocomposites of NiS_2 and $NiSO_4(H_2O)_6$ using hydrothermal method. The various techniques confirmed the production of nanocomposites. XRD confirms the structure of $NiSO_4(H_2O)_6$ was monoclinic and NiS_2 was anorthic, size stain plot and Williamson Hall plot revealed the value of crystallite size and strain. UV-visible spectroscopy disclosed the absorbance in the visible region. The determined bandgap was found to be 1.06 eV. The Refractive index was calculated to be 3.32 which suggests the optical properties of the sample. The SEM images revealed the formation of nanocomposites on the surface of carbon nanospheres.

Acknowledgments: The authors gratefully acknowledge essential resources provided by Prof. Anand Shrivastava, Vice Chancellor of Netaji Subhas University of Technology (former Netaji Subhas Institute of Technology, University of Delhi).

Conflicts of interest or competing interests: No conflicts of interest exist among the authors.

References

[1] P. Phogat, R. Jha, and S. Singh, “Impedance Study of Zinc Sulphide Quantum Dots via One Step Green Synthesis”.

[2] C. V. V. M. Gopi, S. Srinivasa Rao, S. K. Kim, D. Punnoose, and H. J. Kim, “Highly effective nickel sulfide counter electrode catalyst prepared by optimal hydrothermal treatment for quantum dot-sensitized solar cells,” *J. Power Sources*, vol. 275, pp. 547–556, 2015, doi: 10.1016/j.jpowsour.2014.11.038.

[3] M. A. Agoro and E. L. Meyer, “Roles of TOPO Coordinating Solvent on Prepared Nano-Flower/Star and Nano-Rods Nickel Sulphides for Solar Cells Applications,” *Nanomaterials*, vol. 12, no. 19, 2022, doi: 10.3390/nano12193409.

[4] J. Lin *et al.*, “Rational construction of core–shell Ni3S2@Ni(OH)2 nanostructures as battery-like electrodes for supercapacitors,” *Inorg. Chem. Front.*, vol. 5, no. 8, pp. 1985–1991, Aug. 2018, doi: 10.1039/C8QI00347E.

[5] S. Keerthana and A. Kumar, “Potential risks and benefits of zinc oxide nanoparticles: a systematic review,” *Crit. Rev. Toxicol.*, vol. 50, no. 1, pp. 47–71, Jan. 2020, doi: 10.1080/10408444.2020.1726282.

[6] X. Liu, L. Jia, G. Fan, J. Gou, S. F. Liu, and B. Yan, “Au nanoparticle enhanced thin-film silicon solar cells,” *Sol. Energy Mater. Sol. Cells*, vol. 147, pp. 225–234, Apr. 2016, doi: 10.1016/J.SOLMAT.2015.12.004.

[7] Shreya, P. Phogat, R. Jha, and S. Singh, “Elevated Refractive Index of MoS2 Amorphous Nanoparticles with a Reduced Band Gap Applicable for Optoelectronics,” pp. 431–439, 2023, doi: 10.1007/978-981-99-2349-6_39/COVER.

[8] Q. Yang *et al.*, “In Situ Formation of Co9S8 Quantum Dots in MOF-Derived Ternary Metal Layered Double Hydroxide Nanoarrays for High-Performance Hybrid Supercapacitors,” *Adv. Energy Mater.*, vol. 10, no. 7, p. 1903193, Feb. 2020, doi: 10.1002/AENM.201903193.

[9] Z. Zheng *et al.*, "Boosting the electrocatalytic activity of amorphous molybdenum sulfide nanoflakes via nickel sulfide decoration," *Nanoscale*, vol. 11, no. 47, pp. 22971–22979, Dec. 2019, doi: 10.1039/C9NR05916D.

[10] R. Pothu *et al.*, "Nickel sulfide-based energy storage materials for high-performance electrochemical capacitors," *Rare Met.*, vol. 40, no. 2, pp. 353–373, 2021, doi: 10.1007/s12598-020-01470-w.

[11] Dipti, P. Phogat, Shreya, D. Kumari, and S. Singh, "Fabrication of tunable band gap carbon based zinc nanocomposites for enhanced capacitive behaviour," *Phys. Scr.*, vol. 98, no. 9, 2023, doi: 10.1088/1402-4896/acf07b.

[12] A. Yadav, Shreya, and N. K. Puri, "Preliminary Observations of Synthesized WS2 and Various Synthesis Techniques for Preparation of Nanomaterials," *Lect. Notes Mech. Eng.*, pp. 546–556, 2023, doi: 10.1007/978-981-16-9523-0_61/COVER.

[13] P. Phogat, Shreya, R. Jha, and S. Singh, "Optical and Microstructural Study of Wide Band Gap ZnO@ZnS Core–Shell Nanorods to be Used as Solar Cell Applications," pp. 419–429, 2023, doi: 10.1007/978-981-99-2349-6_38.

[14] P. Phogat, Shreya, R. Jha, and S. Singh, "Diffusion Controlled Features of Microwave Assisted ZnS/ZnO Nanocomposite with Reduced Band Gap," *ECS J. Solid State Sci. Technol.*, vol. 12, no. 3, p. 34004, 2023, doi: 10.1149/2162-8777/acc426.

[15] S. Sharma, P. Phogat, R. Jha, and S. Singh, "Electrochemical and Optical Properties of Microwave Assisted MoS2 Nanospheres for Solar Cell Application," *Int. J. Smart Grid Clean Energy*, vol. 12, no. 3, pp. 66–72, 2023, doi: 10.12720/sgce.12.3.66-72.